5.1. Introduction

In recent years, nanocrystalline manganites (also known as nano manganites) have been given much attention by the researchers due to their unexpected properties and phenomena which are not shown by their bulk counterpart such as suppression of charge ordering (CO), appearance of Griffiths phase (GP), evolution of exchange bias (EB) effect, and existence of reentrant spin glass (RSG) state [Shankar et al. (2015); Shankar et al. (2018); Markovich et al. (2014); Markovich et al. (2010)]. Essentially, systems of magnetic nanoparticles have been of huge interest due to their fantastic physical behaviors and their technological applications, examples are magnetic sensors, magnetic recording media (MRM), magnetic refrigeration, permanent magnets, magnetic resonance imaging (MRI), magnetically assisted drug delivery, hyperthermia etc. [Leontie et al. (2018); Manh et al. (2014); Wang et al. (2000)]. As discussed in chapter 1, amongst the various perovskite manganites, the mixed-valence perovskite manganites are most important materials because of their colossal magnetoresistance (CMR) [Ramirez (1997); Hu et al. (2014)]. The phenomena of CMR in mixed-valence manganites was first explained by C. Zener on the basis of double exchange (DE) interactions among Mn^{3+} and Mn^{4+} cations through O^{2-} anions. But this model was unable to explain the enhancement in electrical resistivity above Curie temperature T_C [Zener (1951); Hazzez et al. (2016)]. Since the strength of DE interactions strongly depends on the ratio of Mn^{3+} and Mn^{4+} cations, the variation in the above ratio causes variation in DE interactions [Kumar et al. (2019)]. Besides this, their physical behaviors is governed by two common extensive classes of competing effects, that is competition between ‘the orbital and charge orders that lead to insulating and generally antiferromagnetically ordered ground state’ and the ‘DE interactions that lead to metallic and ferromagnetically ordered ground state’ [Rao (2000); Rao et al. (2000);

Zhang (2007)]. Due to this strong competition between charges, orbital, lattices and spin degrees of freedom, these materials have became a topic of both theoretical and experimental examinations.

Recently, Giri et al. (2014b) studied magnetic properties of nanoparticles (NPs) of $Sm_{0.5}Ca_{0.5}MnO_3$ (SCMO-50) manganite in terms of rigorous measurement of linear and non-linear ac susceptibilities, time-dependent relaxation and aging phenomena. These measurements confirm that the NPs of SCMO-50 are showing mixed phase glassy-behavior in the low temperature region. It has been reported that the SCMO-50 NPs are exhibiting Griffith phase above Curie-temperature (T_C) having FM spin-spin correlation, without acquiring any spontaneous magnetization (M_0) due to the suppression of CO/AFM state with critical exponent $\lambda = 0.85(2)$ [Giri et al. (2014b)]. Hintze et al. (2017) studied size-dependent structural and magnetic properties of $La_{1-x}Sr_xMnO_3$ with x = 0.35 and 0.50 nanoparticles. They observed that the unit-cell volume and Mn-O bond length increase with decreasing particle size, while the Mn-O-Mn bond angle was found to decrease. The FM ordering temperature T_C decreases extensively by up to 20 % with decreasing particle size of the studied manganites [Hintze et al. (2017)].

In this chapter, we have studied the size-dependent structural and magnetic properties of $Nd_{0.7}Ba_{0.3}Mn_{0.9}Ti_{0.1}O_3$ (NBMTO-10) manganite using Rietveld refinement of powder XRD data, and temperature and magnetic field dependent magnetization measurements. The spin dynamic of the NBMTO-10 manganite was studied by using temperature dependent ac susceptibility measurements. The Rietveld structure analysis reveals that variation in crystallite size does not lead to any structural transition except an increase in unit cell volume with increasing crystallite size. Magnetic measurements show that NBMTO-10 undergoes PM-FM transition and in the low-temperature region

exhibits coexistence of FM and AFM ordering. AC susceptibility measurements reveal that the samples of NBMTO-10 manganite display multiple transitions.

5.2. Experimental Details

The nanocrystalline NBMTO-10 perovskite manganite of different particle sizes was synthesized using combustion synthesis method. The details of the sample synthesis process are given in Chapter 2. The as prepared powder sample of NBMTO-10 manganite was divided into several parts and calcined at different temperatures ranging from 800°C to 1300°C at an interval of 100°C for 6 hrs in a muffle furnace and cooled down to room temperature in open air. Samples of NBMTO-10 calcined at 800, 900, 1000, 1100 and 1300°C are denoted by C8, C9, C10, C11, and C13, respectively throughout this chapter. The room temperature X-ray diffraction (XRD) pattern of calcined powders were recorded using Rigaku Miniflex Cu target XRD machine in the 2θ range 20°-120° with a scan rate of 2°/min. The structural analysis was done using Rietveld refinement with the help of FullProf Suite [Carvajal (1993)]. Microstructural and elemental analysis of the NBMTO samples were carried out using high-resolution scanning electron microscopy (HR-SEM) and energy dispersive X-ray spectroscopy (EDS) (FEI, Nova NanoSEM 450). The magnetic properties of the samples were measured using superconducting quantum magnetometer design (SQUID), vibrating sample magnetometer (VSM), magnetic property measurement system (MPMS-3). The temperature dependence of magnetization was measured in the zero field cooled (ZFC) and field cooled (FC) modes in the temperature range of 2-300 K at the constant field of 200 Oe. The field dependence of magnetization was measured in the field of -60 kOe to +60 kOe. The temperature and frequency dependence of ac susceptibility measured at 10, 100 and 1 kHz in the temperature range of 2-390 K.

5.3. Results and Discussion

5.3.1. Structural and Microstructural Studies

5.3.1.1. Structure Analysis: Rietveld Refinement

The room temperature powder X-ray diffraction patterns of NBMTO-10 manganite calcined at several temperatures are shown in **Fig. 5.1(a)**. All the XRD patterns show the crystalline nature of the samples. All samples are crystallized in single orthorhombic phase; no secondary impurity phase was detected except the C8 sample which shows small impurity peaks of $BaMnO_3$ at $2\theta = 25.8°$ and Mn_3O_4 at $2\theta = 31.4°$ in the XRD pattern marked by (#) and (*) symbols, respectively, as shown in **Fig. 5.1(a)**. The peak broadening in the XRD patterns decreases with increasing calcination temperature, which indicates an increase in crystallite size. A detailed analysis of peak broadening in the XRD pattern is presented in the upcoming section. The powder XRD patterns of calcined powder samples were examined for crystal structure using Rietveld refinement technique [Young (1993)]. All the diffraction patterns can be indexed using orthorhombic crystal structure with *Imma* space group. In the refinement process, we considered substitution of Ti^{4+}-ions at Mn-site and Ba^{2+}-ions at Nd-site in NBMTO-10 manganite.

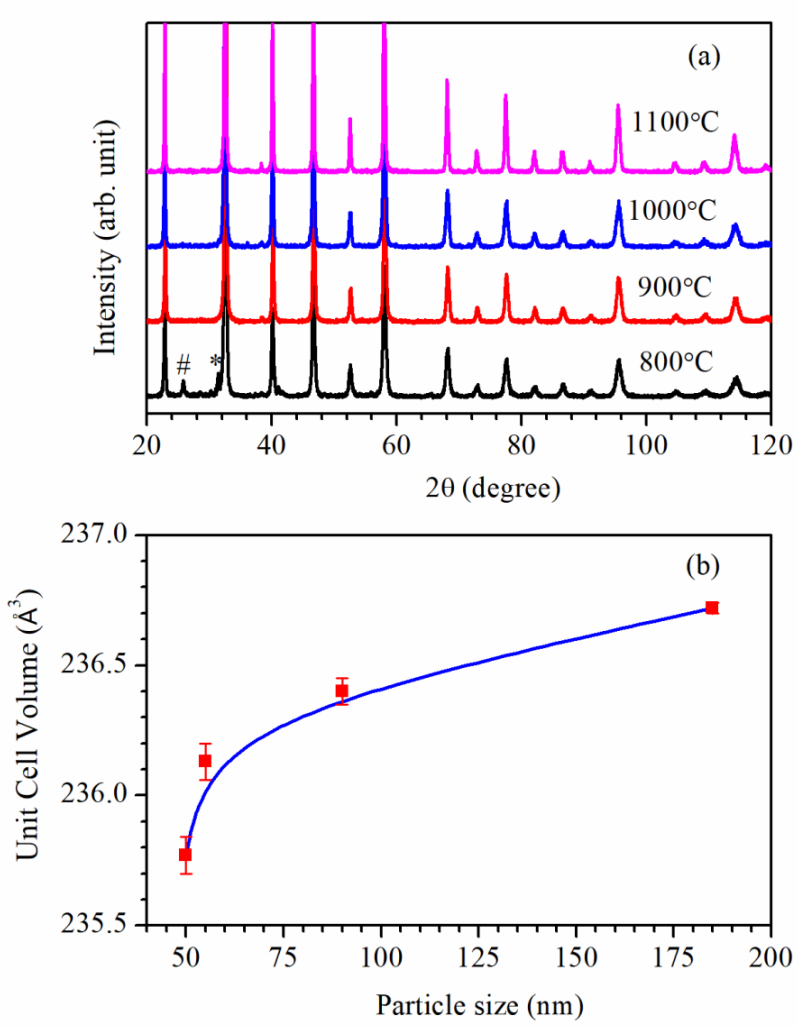

Figure 5.1: (a) Room temperature XRD patterns of $Nd_{0.7}Ba_{0.3}Mn_{0.9}Ti_{0.1}O_3$ manganite calcined at various temperatures ($^{\#}$=$BaMnO_3$; *=Mn_3O_4). (b) Variation in unit cell volume as a function of particle size.

In the Rietveld refinement using orthorhombic phase with *Imma* space group, $Mn^{3+}/Mn^{4+}/Ti^{4+}$ ions occupy *4(b)* site at (0, 0, 1/2), Nd^{3+}/Ba^{2+} and O^{2-}(1) ions occupy *4(e)* site at (0, 1/4, δz) and O^{2-}(2) ions occupy *8(g)* site at (3/4, δy, 1/4) [Kumar et al. (2019)]. The values of lattice constants and unit cell volume obtained after Rietveld structure refinement are listed in **Table 5.1**. The unit cell volume of the samples increases from 235.77(6) $Å^3$ for C8 to 236.73(2) $Å^3$ for C11 with increasing calcination temperature. **Fig. 5.1(b)** displays variation in unit cell volume as a function of particle

size (calculated from HR-SEM micrographs). The Rietveld fits for the powder X-ray diffraction patterns for the experimental and calculated XRD profiles are shown in **Fig. 5.2** for all the samples of NBMTO-10 manganite. The circular dots show the experimental data while the calculated data is shown by overlapping continuous curve. The lowest curve shows the difference between experimental and calculated XRD patterns. The vertical bars show the positions of Bragg's reflection in the XRD pattern.

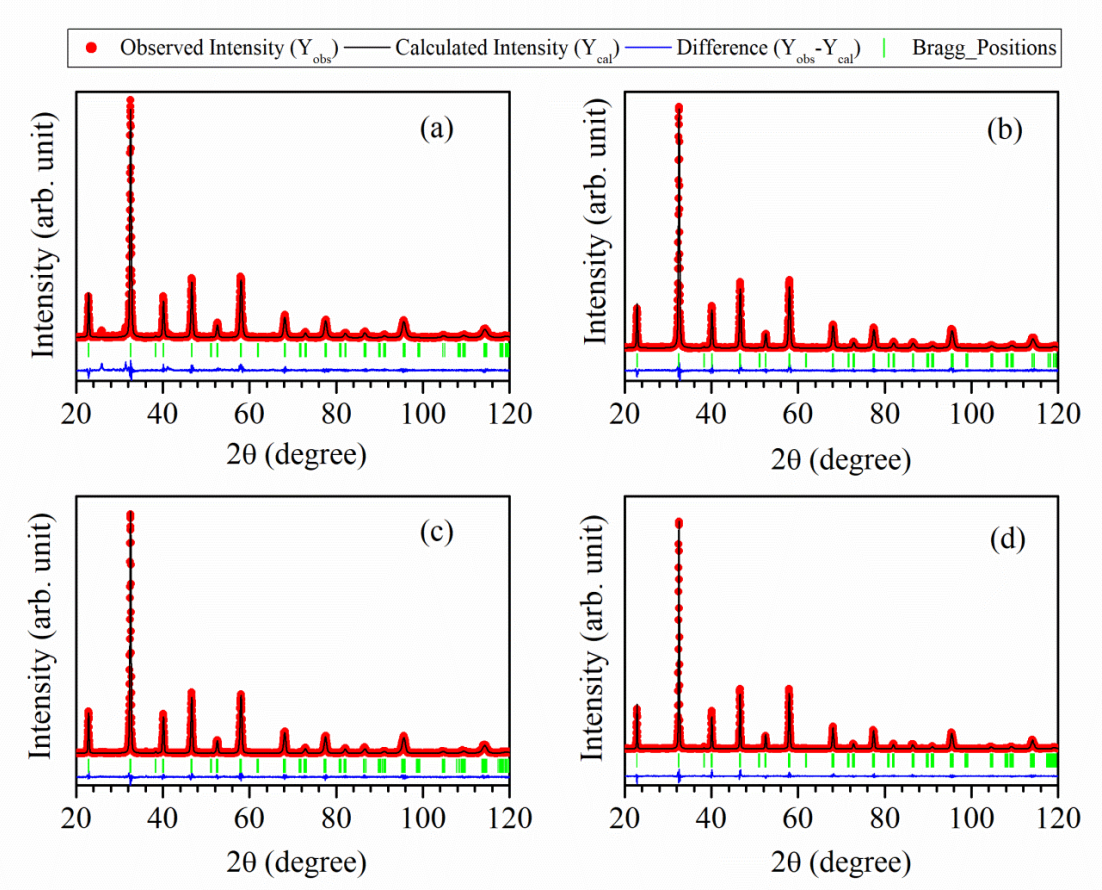

Figure 5.2: The Rietveld fits between observed and calculated XRD patterns for (a) C8, (b) C9, (c) C10 and (d) C11 samples of NBMTO-10 manganite.

Table 5.1: Average values of particle & crystalline size, lattice strain, lattice constants and unit cell volume of NBMTO-10 manganite samples calcined at different temperatures.

Sample	Crystallite/Particle size (nm)			Lattice constant (Å)			Unit cell volume ($Å^3$)	Lattice strain (ε)
	d_{D-S}	d_{W-H}	d_{HR-SEM}	a	b	c		
C8	25.68	47.94	50	5.4998(9)	7.7841(9)	5.5074(7)	235.77(6)	2.68×10^{-3}
C9	30.94	49.14	55	5.5071(8)	7.783(1)	5.5086(9)	236.13(4)	2.03×10^{-3}
C10	34.96	56.43	90	5.5222(8)	7.7840(6)	5.4995(7)	236.40(5)	1.57×10^{-3}
C11	68.54	75.75	185	5.5048(3)	7.7855(5)	5.5236(3)	236.73(2)	0.87×10^{-3}

5.3.1.2. Microstructural and Elemental Analysis

The microstructural peak broadening in the XRD profiles has been investigated using Debye-Scherrer (D-S) and Williamson-Hall (W-H) methods. First, we employed D-S method to study the peak broadening in the form of crystallite size. Crystallite size of the samples estimated through D-S method using the formula given by the Equation (5.1):

$$d_{D-S} = k\,\lambda/\beta_s \cos\theta \tag{5.1}$$

Here, k is a constant equal to 0.89; λ is the wavelength of the X-ray radiation; β_s and θ are FWHM and Bragg angle of the most intense peak in the XRD pattern, respectively [Kumar et al. (2019)]. Since the broadening in peak contains both broadenings due to the crystallite size of the sample and instrument, we have to subtract instrumental broadening from the measured peak broadening, to only encounter the broadening due to crystallite size. To determine the instrumental broadening, we recorded the XRD pattern of a standard silicon (Si) sample. The corrected FWHM was used to estimate the crystallite size given by Equation (5.2) [Zak et al. (2011)]:

$$\beta_s = [\beta_{measured} - \beta_{intrument}]^{1/2} \tag{5.2}$$

The values of crystallite sizes calculated using equation (5.1) were found to be 25.68, 30.94, 34.96 and 68.54 for the samples C8, C9, C10 and C11, respectively, which increase exponentially with increasing calcination temperature (see **Fig. 5.3**(e)).

Further, D-S method used for the calculation of crystallite size doesn't consider the contribution of lattice strain present in the peak broadening. Therefore, we used Williamson-Hall plot method to estimate the peak broadening arising due to crystallite size ($d_{W\text{-}H}$) and lattice strains (ε). Thus, the modified D-S equation can be expressed by the equation (5.3), to estimate the average value of crystallite size and lattice strain:

$$\beta_{hkl} \cos\theta_{hkl} = 0.89\, \lambda/d_{W\text{-}H} + 4\varepsilon \sin\theta_{hkl} \qquad (5.3)$$

Here, β_{hkl} is FWHM of the Bragg peaks, θ_{hkl} is Bragg's angle corresponding to (hkl) plane and λ is the wavelength of the radiation used for recording XRD patterns [Kumar et al. (2018a)]. **Figs. 5.3**(a-d) demonstrate W-H plots for the samples C8, C9, C10 and C11, respectively. The average values of the crystallite sizes estimated from W-H plot method was found to be 47.94, 49.14, 56.43 and 75.75 nm for the samples C8, C9, C10 and C11, respectively, which increases exponentially as a function of calcination temperature (see **Fig. 5.3**(e)). However, the contribution of lattice strain in the peak broadening diminishes linearly with an increase in crystallite size (see **Fig. 5.3**(f)). The values of lattice strain decreases from 2.68×10^{-3} to 0.87×10^{-3} as crystallite size of NBMTO-10 increases from 47.94 nm to 75.75 nm. Variation in crystallite size calculated by D-S formula and W-H plot is presented in **Fig. 5.3**(e), however, **Fig. 5.3**(f) shows variation in lattice strain with calcination temperature. The values of crystallite size calculated by the D-S method are larger than the values estimated by W-H plot method as the contribution of strain is also included.

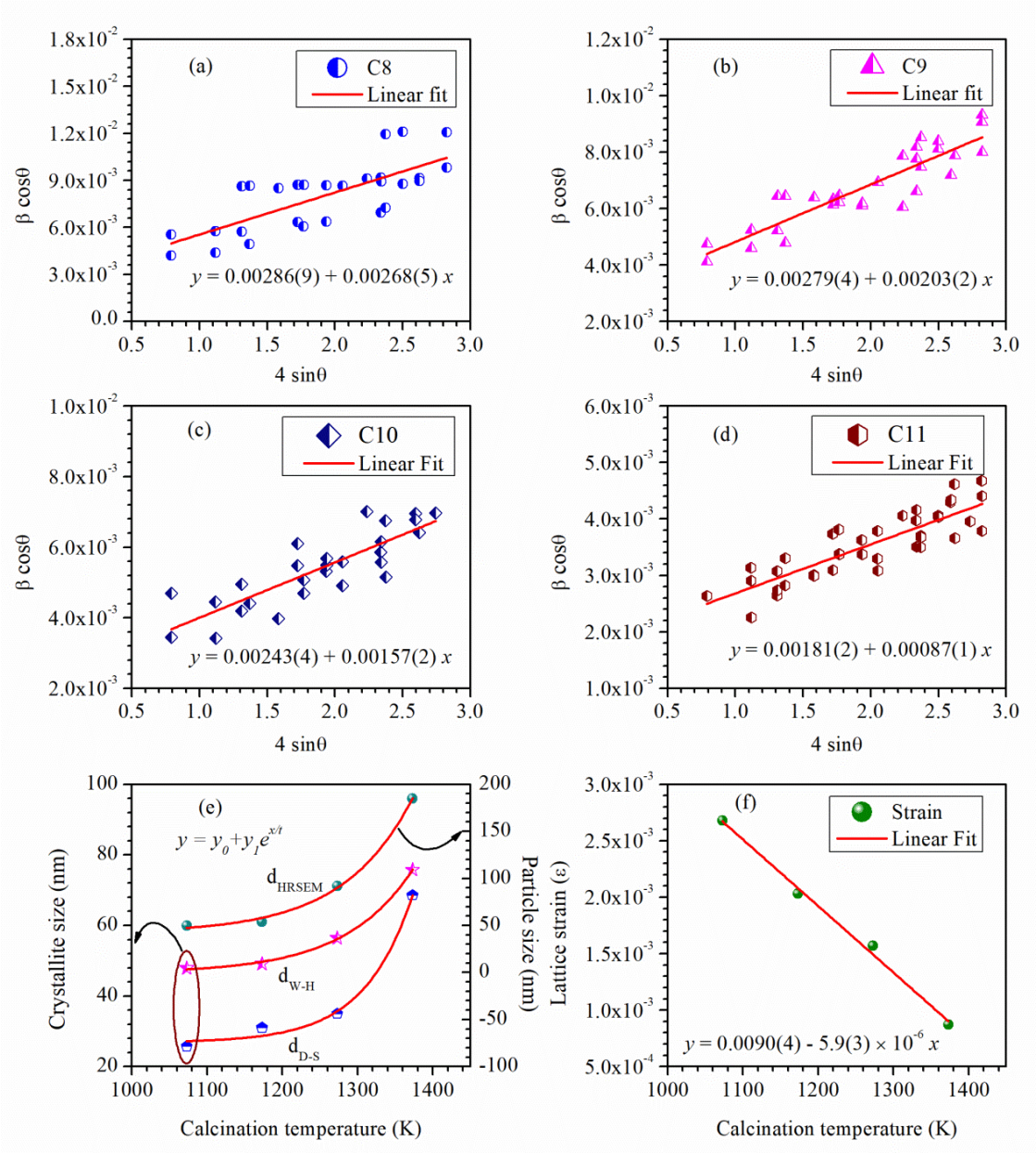

Figure 5.3: Williamson-Hall plots for the samples (a) C8, (b) C9, (c) C10, and (d) C11. Variation in (e) crystallite and particle sizes estimated using D-S & W-H methods and HRSEM micrographs and (f) lattice strain, as a function of calcination temperature.

The typical High-Resolution Scanning Electron Microscopic (HR-SEM) micrographs for 10% Ti-doped $Nd_{0.7}Ba_{0.3}MnO_3$ samples calcined at different temperatures are shown in **Fig. 5.4**. The average particle sizes were estimated using ImageJ software considering as many particles as possible and are found to be

approximately 50, 55, 90 and 185 nm for the samples calcined at 800 (C8), 900 (C9), 1000 (C10), and 1100°C (C11), respectively, which increase exponentially with increasing calcination temperature. The estimated values of particle sizes from HR-SEM images is greater than the respective values of crystallite sizes which point outs that the particles are made up of several nano-crystals. The variation of the particle size with calcination temperature as determined from the HR-SEM is shown in **Fig. 5.3**(e).

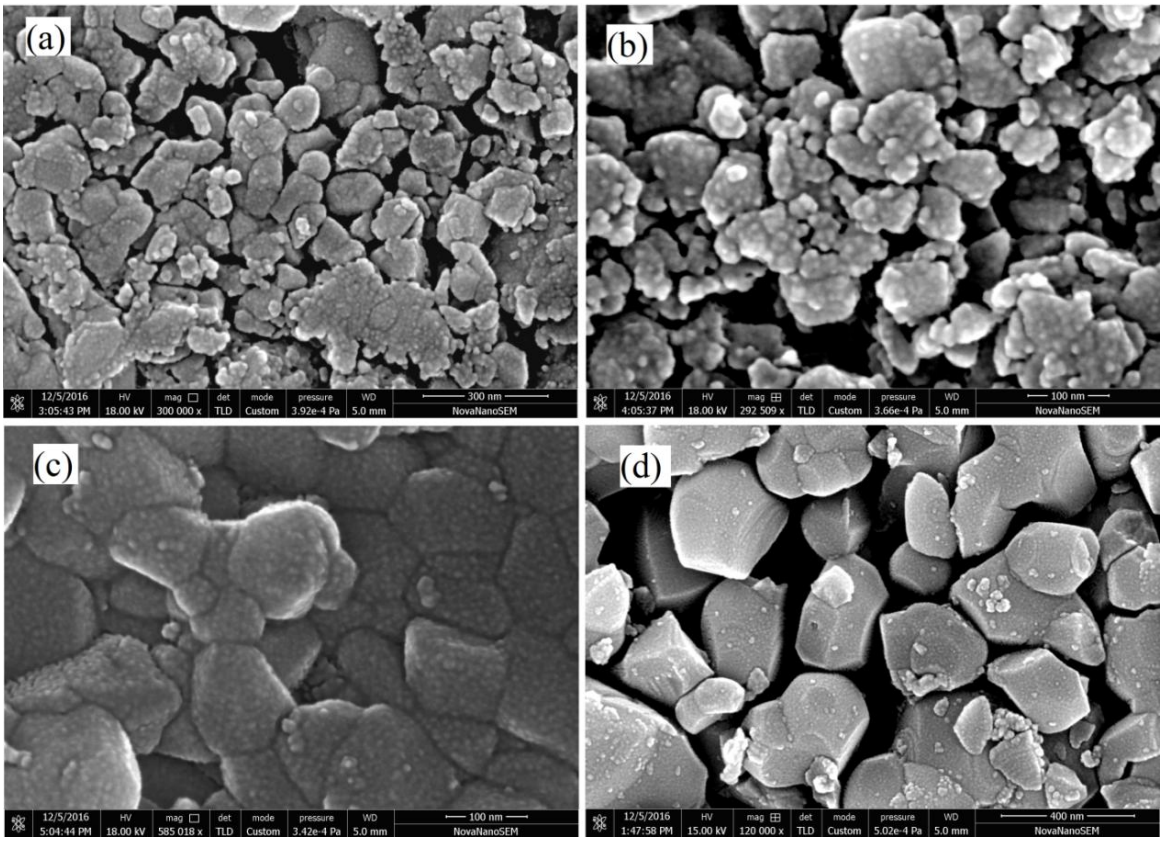

Figure 5.4: HR-SEM micrographs for NBMTO-10 manganite calcined at (a) 800°C, (b) 900°C, (c) 1000°C and (d) 1100°C.

For the elemental analysis of the samples, we recorded the EDS spectra inbuilt in the same HR-SEM system. **Figs. 5.5(a-d)** show EDS spectra of the samples calcined at various temperatures viz. 800, 900, 1000 and 1100°C, respectively. The characteristic peaks present in the EDS spectra corresponding to the constituent elements confirm the

presence of all the elements in the samples i.e. Nd, Ba, Mn, Ti, and O without any impurity. Since all the samples were derived from the same powder obtained after combustion the composition will be same for all the samples calcined at various temperatures.

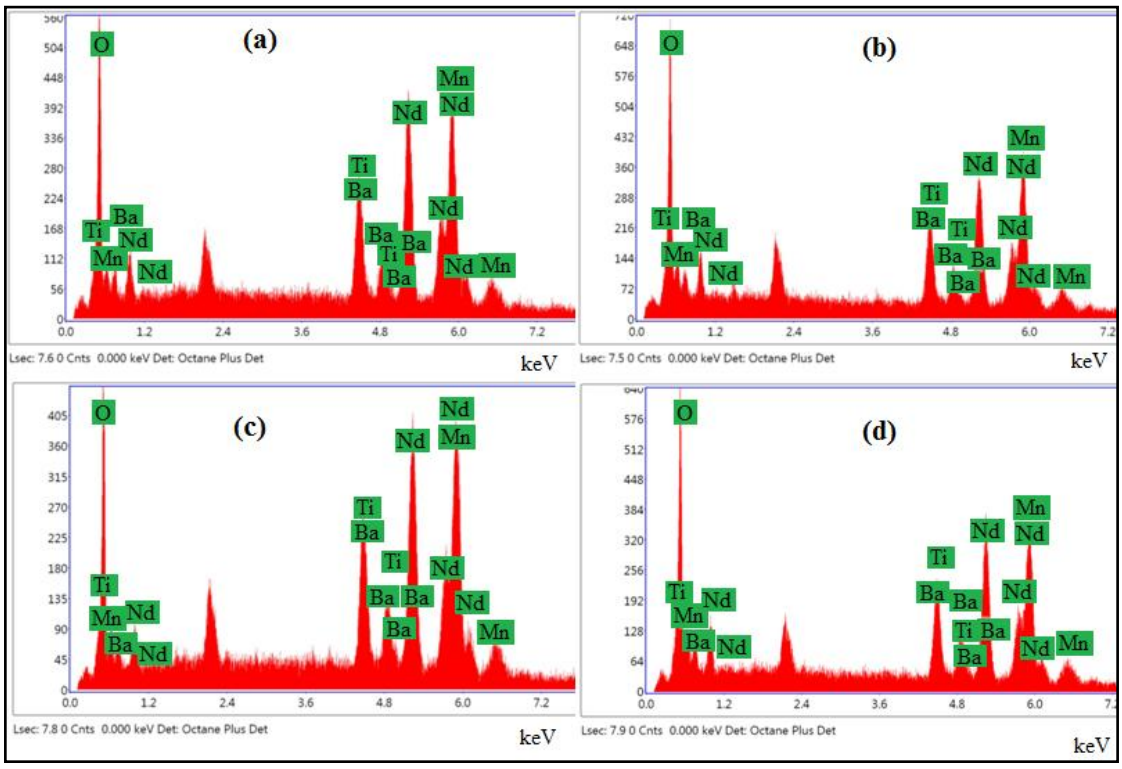

Figure 5.5: The EDS spectra for NBMTO-10 manganite calcined at (a) 800°C, (b) 900°C, (c) 1000°C, and (d) 1100°C.

5.3.2. Magnetic Properties

5.3.2.1. Temperature Dependent Magnetization Studies

The temperature dependence of magnetization (M(T)) curves measured in zero field cooled (ZFC) and field cooled (FC) modes at the constant applied field of H = 200 Oe in the temperature range 2-300 K, are shown in **Fig. 5.6(a)**. The ZFC magnetization (M_{ZFC}) and FC magnetization (M_{FC}) increases with decreasing temperature and M_{ZFC} reaches a maximum value at a characteristic temperature known as blocking

temperature (T_B) and decreases further on decreasing temperature. The M_{FC} for C8 and C10 keep increasing after T_B and for C9 and C11 M_{FC} decreases slowly below T_B. The above observations reveal that M_{ZFC} and M_{FC} bifurcate below an irreversible temperature (T_{irr}) in the low-temperature regime. The magnetization measurement reveals PM to FM transition at Curie temperature (T_C), defined by the anomaly appearing in the dM/dT curve as shown in **Fig. 5.6(b)**. The value of T_C decreases linearly with increasing calcination temperature from 93 K for C8 (800°C) to 59 K for C11 (1100°C), however, the sample calcined at 1000°C (C10) shows highest T_C equal to 106 K irrespective of the others. **Fig. 5.6(c)** shows a variation in T_C as a function of particle size.

The change in the magnetic ordering temperature T_C can be explained by using a double exchange mechanism between Mn^{3+} and Mn^{4+} ions through O^{2-} ion. The overlapping between 3d-orbital of Mn and 2p-orbital of O gives the extent of DE interaction. Since the samples calcined at different temperatures have different unit cell volume and bond lengths, the extent of overlap between orbitals will be different which in turn lead to differing T_C for different samples. In the magnetization curve of the sample C8, we do not get any signal of the ferrimagnetic ordering of Mn_3O_4 having Curie temperature T_C = 42 K [Dwight et al. (1960)] and AFM ordering of $BaMnO_3$ with Neel temperature T_N = 220 K [Korneta et al. (2011)]. Hence, in the computation of effective PM and saturation moments, we do not take account of the contribution of impurity phase of $BaMnO_3$ and Mn_3O_4 in PM and saturation moments, as they are present in very small percentage.

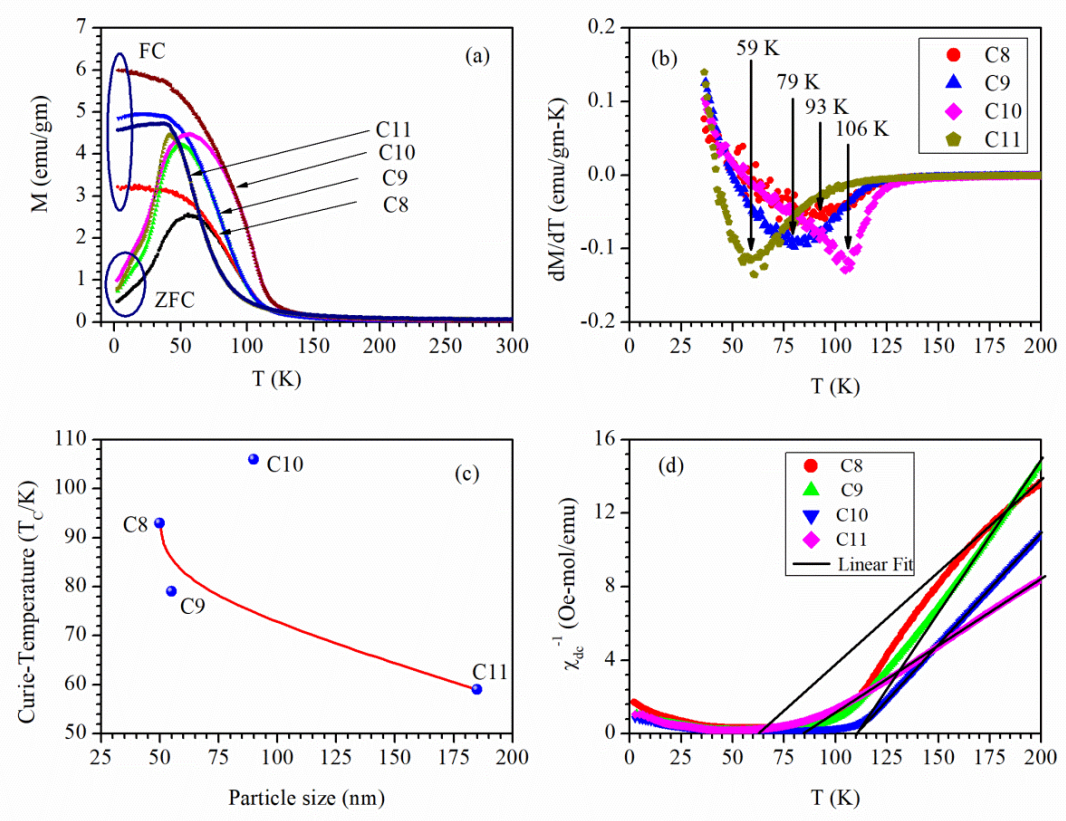

Figure 5.6: (a) Temperature dependence of magnetization curves and (b) dM/dT plots for NBMTO-10 manganite calcined at various temperatures. (c) Variation of Curie temperature (T_C) as a function of calcination temperature. (d) Temperature-dependent inverse dc molar susceptibility for NBMTO-10 manganite.

5.3.2.2. Temperature Dependent Inverse dc Susceptibility Studies

The temperature dependence of inverse dc molar susceptibility (χ_{dc}^{-1}) in the high temperature PM region obeys Curie-Weiss (CW) law, $\chi_{dc}^{-1} = (T - \theta_{CW})/C$, where, C is Curie constant and θ_{CW} is CW temperature. **Fig. 5.7** shows temperature dependent variation of dc molar susceptibility (χ_{dc}^{-1}) for all the samples of NBMTO-10 manganite. The χ_{dc}^{-1} exhibits two linear regions, with different slopes, in the high temperature regime. The first region (designated as R1) is related to the FM transition; while the other (R2) is located at higher temperatures corresponds to AFM transition. The values of C and θ_{CW} parameters obtained from fitting the data in the R1 and R2 regions to the

CW law generate two distinct values. The values of C and θ_{CW} in region R1 are comparable to theoretical values corresponding to Mn^{p+}-ions. Actually, two linearly characteristic regions of $\chi^{-1}(T)$ having distinct C and θ_{CW} values were also observed in $La_{0.7}Ca_{0.3}MnO_3$ nanoparticles [Thanh et al. (2014)] and $LaMn_{1-x}Cu_xO_3$ (x = 0.05-0.30) [Srivastava et al. (2006)].

Fig. 5.6(d) shows the temperature dependence of inverse molar susceptibility for the samples of NBMTO-10 manganites in the FM transition region (R1). The inverse of the slope and intercept to the temperature axis of the straight line fit in the PM region provide the values of Curie constant and CW temperature, respectively which is given in **Table 5.2** for the samples of NBMTO-10 manganite. The Curie constant and effective PM moment of the samples are related by Equation (5.4b) given below:

$$C = \frac{\mu_0}{3k_B}\mu_{eff}^2 \tag{5.4a}$$

$$\mu_{eff}^{exp}(\mu_B) = \sqrt{8C} \tag{5.4b}$$

The experimental values of effective PM moment are given in Table **5.2**. The theoretical value of effective PM moment in the Bohr magneton unit was calculated by the Equation (5.5):

$$\mu_{eff}^{theo}(\mu_B) = \sqrt{0.7\mu_{eff}^2(Nd^{3+}) + 0.7\mu_{eff}^2(Mn^{3+}) + 0.2\mu_{eff}^2(Mn^{4+})} \tag{5.5}$$

Which gives, $\mu_{eff}^{theo}(Nd^{3+}) = 3.62\ \mu_B$, $\mu_{eff}^{theo}(Mn^{3+}) = 4.90\ \mu_B$, $\mu_{eff}^{theo}(Mn^{4+}) = 3.87\ \mu_B$ [Phong et al. (2016a); Kossi et al. (2015); Biswas et al. (2007)]. The value of $\mu_{eff}^{theo}(\mu_B)$ is found to be equal to 5.38 μ_B for NBMTO-10 manganite. The value of $\mu_{eff}^{exp}(\mu_B)$ is larger than the value of $\mu_{eff}^{theo}(\mu_B)$, which may be due to the presence of FM short-range ordering within the PM matrix [Hazzez et al. (2016)].

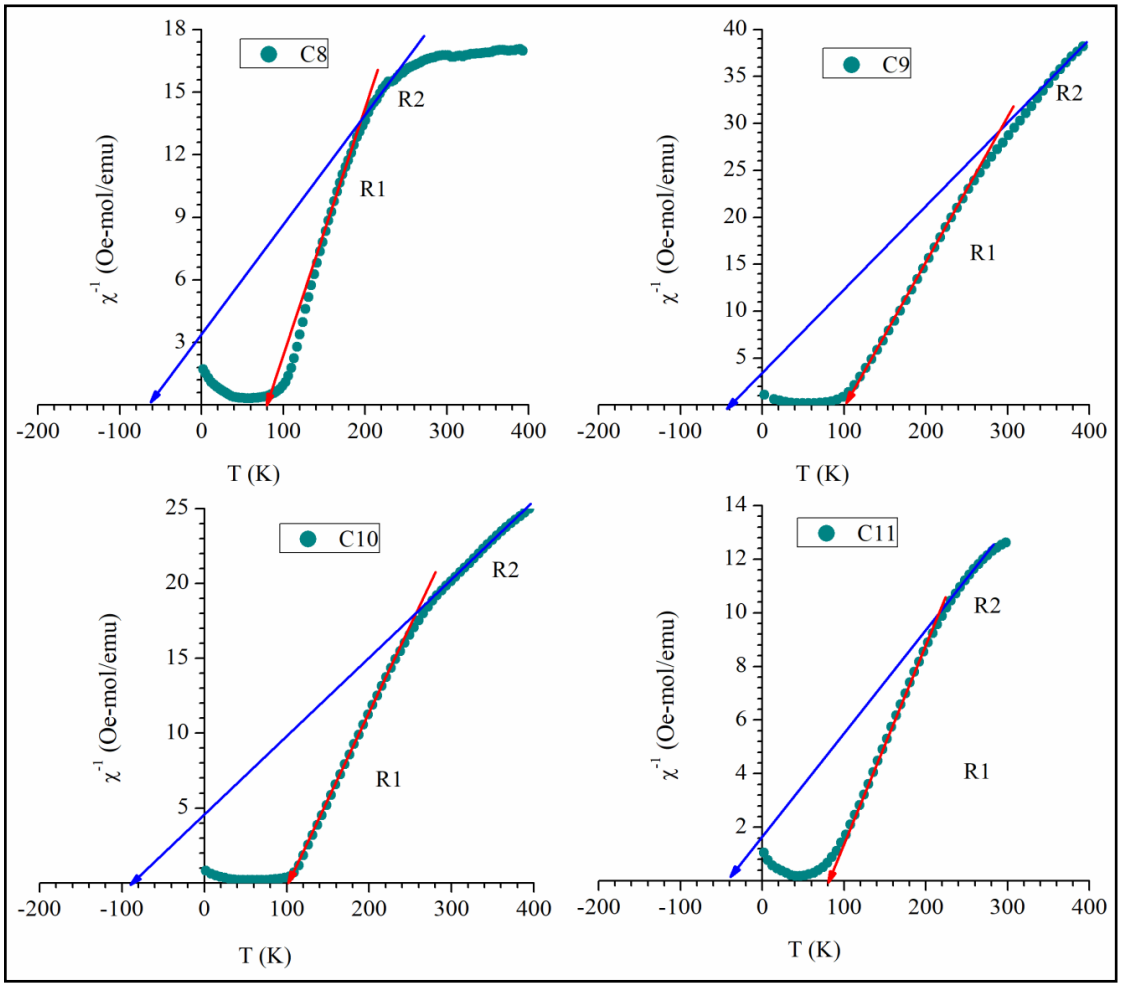

Figure 5.7: (a-d) Inverse of magnetic dc susceptibility for C8, C9, C10 and C11 samples of NBMTO-10 manganite. The straight line fits for the two different linear regions were done by using Curie-Weiss law.

5.3.2.3. Griffiths Phase Analysis

The temperature dependent inverse susceptibility for C8 in region R1 shows downward deviation from CW law as clearly shown in **Fig. 5.9**(a). The downward deviation in the $\chi^{-1}(T)$ is an indication of Griffiths Phase (GP). Onset temperature of the downward deviation in $\chi^{-1}(T)$ is defined as Griffiths' temperature (T_G). The GP corresponds to the temperature region where some short-range FM ordering appears in the PM region, i.e., there is quenching of disordering state (see **Fig. 5.8**). It lies in the

temperature between T_C and T_G ($T_C \leq T \leq T_G$). In this region, $\chi^{-1}(T)$ follows modified CW law given by Equation (5.6):

$$\chi_m^{-1} \propto (T - T_C^R)^{1-\lambda} \tag{5.6}$$

where, T_C^R is critical temperature of random ferromagnet where susceptibility tend to diverge, lies below Griffiths' temperature T_G and above long-range ordering temperature T_C, and λ is exponent for magnetic susceptibility, lies in the range $0 \leq \lambda \leq 1$, which is a measure of deviation from CW law. The selection of the critical temperature T_C^R is very crucial for the accurate determination of λ, to characterize the GP. The reliable values of T_C^R were obtained by Karmakar et al. (2012) following a procedure in which T_C^R is identified as that temperature for which fitting the data in the PM region yielded $\lambda \sim 0$. Though, this approach is effectively equivalent to estimating value of θ_{CW}. Hence, we have chosen $T_C^R = \theta_{CW}$ = 80.4 K. **Fig. 5.9(b)** shows $\log_{10}\chi^{-1}$ vs. $\log_{10}(T/T_C^R - 1)$ plot for the sample C8, the linear portion in the high-temperature region above T_G is attributed to the PM state. Fitting of this PM region with equation (5.6) yielded λ_{PM} = 0. The fitting of χ_m^{-1} in the GP region provided λ_{GP} = 0.926(1). A relatively large values of λ_{GP} point outs the strength of GP in the present sample. Such a large value for λ_{GP} is also reported by several authors in various systems [Giri et al. (2014b)].

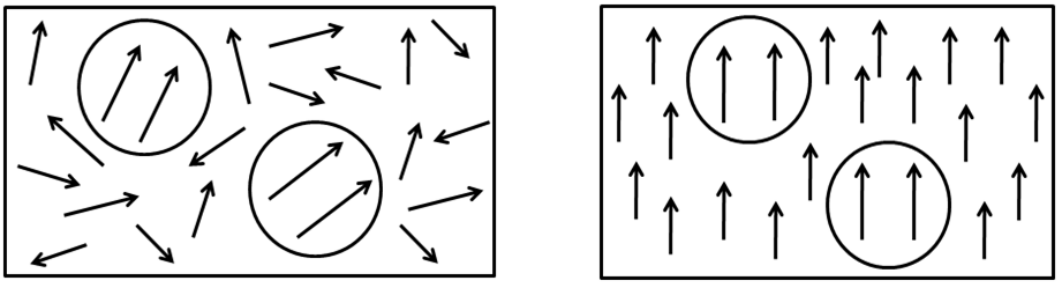

(a) $T_C \leq T \leq T_G$ (b) $T \leq T_C$

Figure 5.8: Ordering of the spins in (a) Griffith's phase region ($T_C \leq T \leq T_G$) and (b) below FM transition ($T \leq T_C$).

Table 5.2: Curie temperature T_C; Curie-Weiss temperature θ_{CW}; Curie constant C; experimental μ_{eff}^{exp} and theoretical μ_{eff}^{theo} effective paramagnetic moments; for NBMTO-10 samples of various particle sizes.

Sample	T_C (K)	θ_{CW} (K)	C (emu-K/Oe-mol)	Effective PM moment (μ_B)	
				Exp.	Theo.
C8	93	60.5	10.13	9.00	5.38
C9	79	104.0	6.38	7.14	5.38
C10	106	103.9	8.48	8.24	5.38
C11	59	85.5	13.51	10.40	5.38

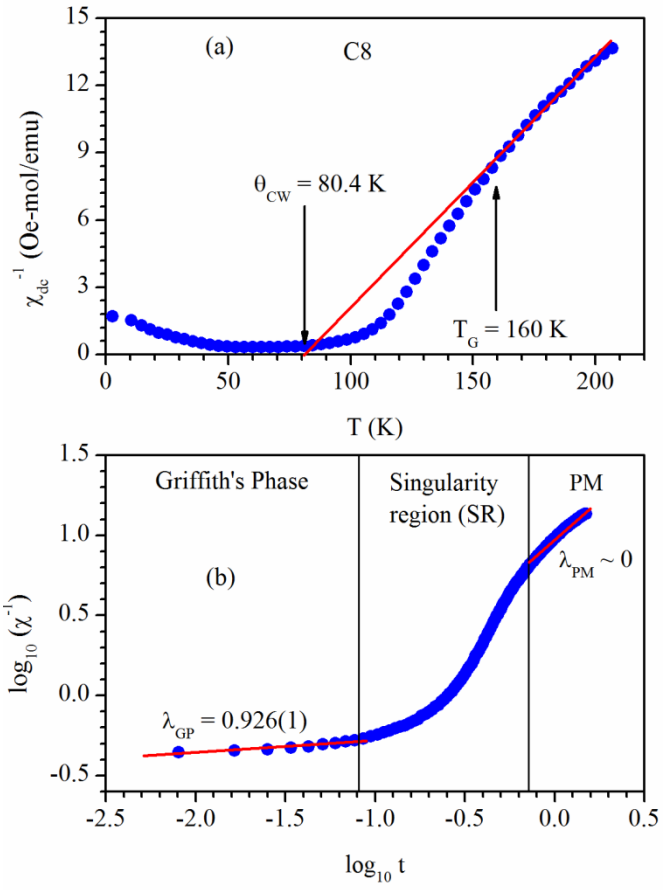

Figure 5.9: (a) Temperature dependent inverse dc susceptibility for C8 sample and (b) log-log plot between $\chi^{-1}(T)$ and reduced temperature (t) for C8 to estimate critical exponent λ_{GP}.

5.3.2.4. Field Dependent Magnetization Studies

The field dependent magnetizations M(H) were measured at 10 K in the magnetic field range from -60 kOe to +60 kOe for the samples of NBMTO-10 calcined at various temperatures. **Fig. 5.10(a)** shows M(H) hysteresis loops for NBMTO-10 perovskite having various particle sizes. In the low magnetic field region, the value of magnetization arises rapidly which confirms the presence of FM ordering, however, in the higher filed region magnetization increases continuously with increase in magnetic field and remains unsaturated even at the higher field of 60 kOe indicating the presence of AFM ordering along with FM ordering at 10 K [Yang et al. (2005)]. The values of remnant magnetization (M_r) and coercive field (H_C) were estimated and found to be M_r = 5.53, 6.40, 9.95 and 9.94 emu/gm and H_C = 1075, 1096, 500 and 960 Oe for C8, C9, C10 and C11 samples respectively. In addition, peak magnetization at 60 kOe and saturation magnetization increases with increasing particle size but the sample having average particle size 90 nm (C10) displays maximum value. Similar unusual behavior of magnetization has been reported in nanocrystalline $Nd_{0.5}Sr_{0.5}MnO_3$ also [Shankar et al. 2018]. **Fig. 5.10(b)** shows the variation of saturation magnetization and magnetization at 60 kOe with particle size of the samples.

Further, to estimate the fraction of FM and AFM ordered regions, we have calculated experimental and theoretical values of saturation moments for various particle sizes of the samples. The experimental value of saturation moment was found out using Equation (5.7):

$$\mu_{sat}^{exp}(\mu_B) = \frac{M_{sat}^{exp} \times M_m}{N_a \times \mu_B} \qquad (5.7)$$

Where, M_{sat}^{exp} and M_m are the experimental value of saturation magnetization and molecular mass of the sample, respectively. Experimental values of μ_{sat}^{exp} were found to be 0.87, 1.04, 2.36 and 1.81 μ_B, respectively. The theoretical spin-only value of

saturation moment was calculated considering complete alignments of the spins of Mn^{4+} and Mn^{3+} ions and assuming dilution effect of Ti^{4+} ions using Equation (5.8) given below:

$$\mu_{sat}^{theo}(\mu_B) = 0.7M_{Mn^{3+}} + 0.2M_{Mn^{4+}} + 0.1M_{Ti^{4+}} \quad (5.8a)$$

$$\mu_{sat}^{theo}(\mu_B) = 2\mu_B\left[0.7 \times \frac{4}{2} + 0.2 \times \frac{3}{2} + 0.1 \times 0\right] \quad (5.8b)$$

It is found to be equal to 3.4 μ_B for single formula unit. The fraction of ferromagnetism and antiferromagnetism were estimated and is given in **Table 5.3**. FM fraction increases with increasing particle sizes, whereas, the sample with a particle size 90 nm (cal. at 1000°C) displays maximum FM (60 %) and minimum AFM (40 %) components.

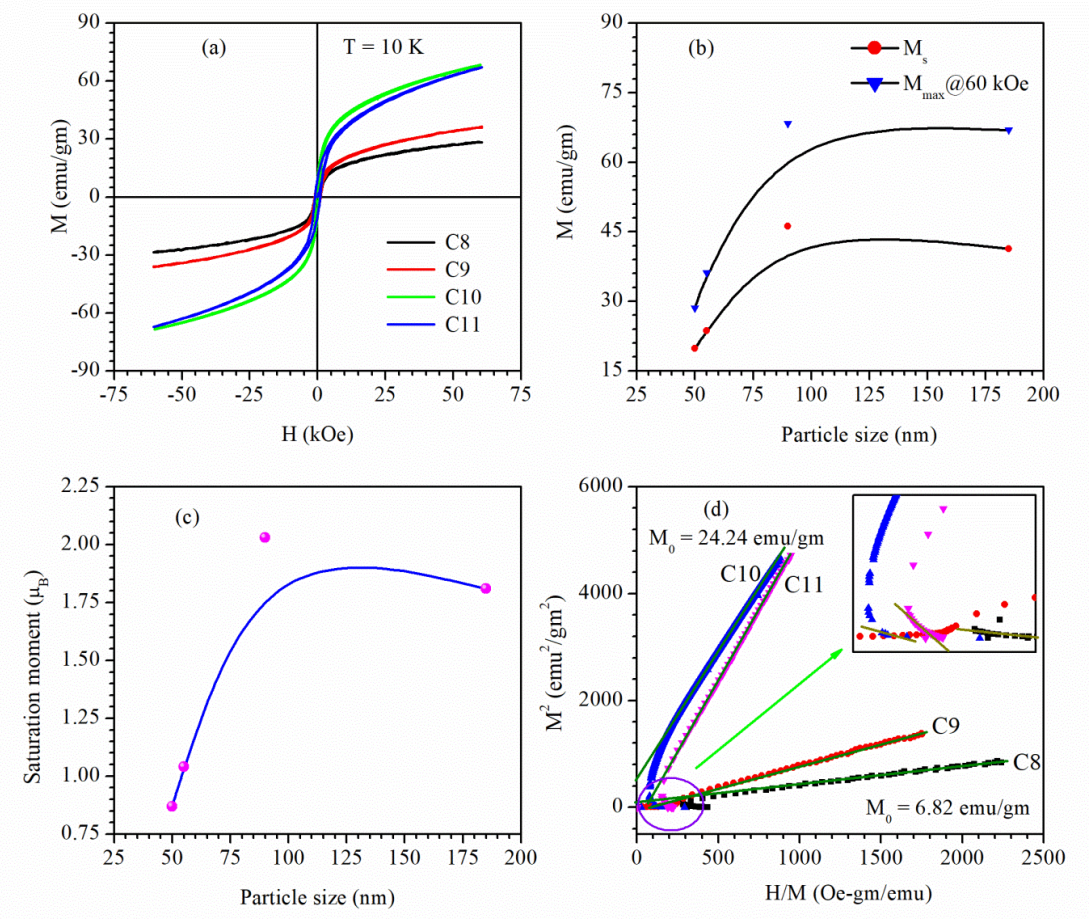

Figure 5.10: (a) Magnetic hysteresis loops for C8, C9, C10 and C11 at 10 K. Variation in (b) M_s and M_{max} at 60 kOe and (c) saturation moment at 10 K as a function of particle size. (d) Arrott's plots for C8, C9, C10 and C11 samples at 10 K.

The type of magnetic transition was identified by using Banerjee criterion [1964]. According this criterion, the magnetic transition is of second order if all the isothermal Arrott's plots M^2 vs. H/M have a positive slope. Conversely, if some of the isothermal Arrott's curves show negative slope in some region, the transition is of first order [Banerjee (1964); Ho et al. (2016)]. **Fig. 5.10**(d) shows Arrott's plots for different samples of NBMTO-10 manganite. Insets of **Fig. 5.10**(d) show zoomed view of Arrott's plots in the low value region of H/M. The slope of the Arrott's plots for NBMTO-10 manganite in higher field regions is positive, conversely, in low field region at some points slope is negative. This reveals that magnetic transition of the samples of NBMTO-10 manganite is of first order in low field region and is of second order in high field region. A similar behavior of magnetic transition was observed in Tb^{3+} doped $La_{0.5}Ca_{0.5}MnO_3$ manganite, which exhibits first order magnetic transition in the low field region, and switches to second order magnetic transition for the higher magnetic field above 10 T [Doshi et al. (2011)]. At high H/M values, the Arrott's plots are straight lines, which intersect M^2-axis (H = 0). These features indicate existence of long-range FM ordering. The value of magnetization corresponding to the intercept at H = 0 is known as spontaneous magnetization M_0 for ferromagnetism. The values of M_0 at 10 K were found to be 6.82 and 24.24 emu/gm for C8 and C10, respectively.

5.3.2.5. Temperature Dependent ac Susceptibility Studied

The real part of the temperature dependent ac susceptibility $\chi'(T)$ in the frequency range 10 Hz to 1 kHz for NBMTO-10 manganite calcined at different temperatures is shown in **Figs. 5.11**(a-d). **Figs. 5.11**(e-h) present the imaginary part of the ac susceptibility $\chi''(T)$ at 10 and 100 Hz. The real part of the ac susceptibility for the samples C8, C9, and C10 exhibit a broad peak. The peak corresponding to maximum value of $\chi'(T)$ shifted towards the higher temperature side with increasing measuring

frequency. This feature may correspond to spin-glass clusters or superparamagnetic (SPM) nature of the samples. To confirm the actual nature of the inhomogeneous magnetic behavior, we calculated a theoretical parameter α, defined by Equation (5.9):

$$\alpha = \frac{\Delta T_f}{T_f \, \Delta \log_{10} f} \tag{5.9}$$

Where, T_f is freezing temperature corresponding to zero frequency, ΔT_f shift in freezing temperature and $\Delta \log_{10} f$ is a change in $\log_{10} f$ [Sahoo et al. (2016); Toro et al. (2013)]. The value of temperature corresponding to the maxima peak is referred to as freezing temperature and is denoted by T_f. The values of T_f for all samples vary exponentially with increasing frequency (f) (see **Figs. 5.12**(a-d)). Thus, a plot between $\log_{10} f$ and T_f produces a straight line as shown in **Fig. 5.12**(e). **Fig. 5.12**(f) shows a variation in freezing temperature at zero frequency as a function of calcination temperature, which is consistent with the variation in Curie temperature. The values of α for all the samples were investigated and found to be 0.007, 0.012, 0.005 and 0.007 for C8, C9, C10, and C11, respectively. The value of α varies from 0.005 to 0.01 for the metallic spin-glass system and for insulating spin glass system 0.06 to 0.08 [Sahoo et al. (2016)]. Mahendiran and coworkers [Mahendiran et al. (2003)] and Mydosh [Mydosh (1993)] estimated the values of α for various systems. They found α ~ 0.005-0.01 for spin glasses, α ~ 0.06-0.09 for Fe nanoparticles embedded in amorphous Fe_2O_3 and Al_2O_3 particles, α ~ 0.03-0.06 for the cluster glass compound $La_{0.5}Sr_{0.5}CoO_3$, α < 0.05 for the A-site doped rare-earth manganites and α > 0.1 for SPM and complex magnetic systems [Roy et al. (2008)]. In the present study the value of α lies in the range 0.005-0.01, this suggests that the investigated systems are falling in the category of metallic spin-glass.

Further, for all samples of NBMTO-10, the imaginary part of ac susceptibility χ"(T) exhibit a local maxima at same temperature near ~10 K which is frequency independent transition corresponding to ordering of the Nd^{3+}-ions (T_{Nd}). There is also a

global sharp maximum peak close to irreversible temperature (T_{irr}) referred as T_f for $\chi''(T)$ which is frequency dependent and shifts towards higher temperature side with increasing frequency consistent with real part of ac susceptibility $\chi'(T)$.

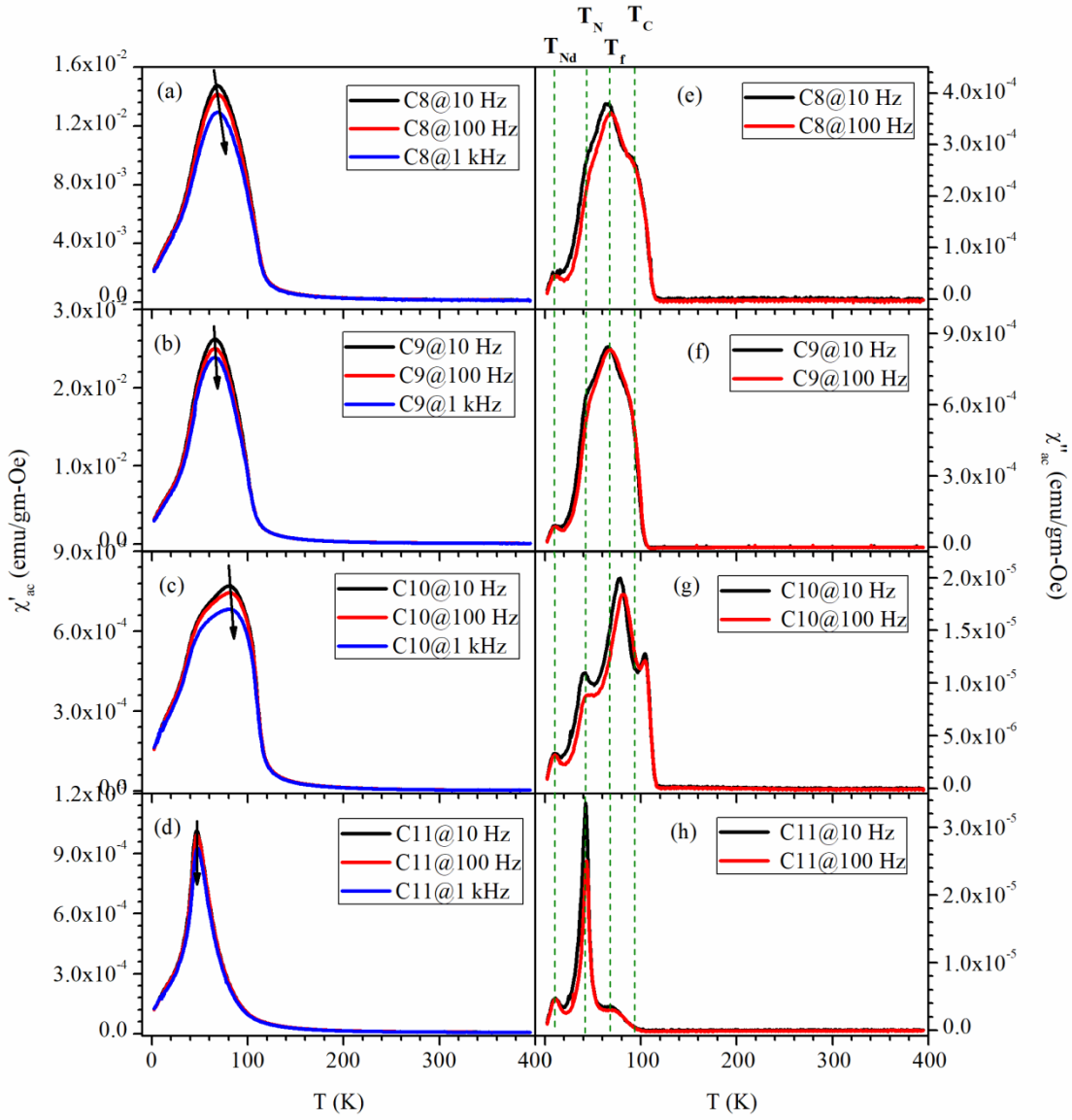

Figure 5.11: Temperature-dependent real part (a)-(d) and imaginary part (e)-(h) of ac susceptibility for the samples C8, C9, C10, and C11 measured at different frequencies, respectively.

The $\chi''(T)$ for the samples C8 and C9 displays two shoulder peaks on either side of the global maxima peak related to T_f. But for the sample C10 these peaks are sharp and well resolved. The anomaly occurring on the lower temperature side of the T_f corresponds to AFM transition (T_N) due to super-exchange interaction between Mn^{3+} and Mn^{3+} ions, while, the anomalous peak occurring n the higher temperature side corresponds to PM to FM transition (T_C). However, $\chi''(T)$ for the sample C11 exhibits AFM and Nd^{3+}-ions ordering at same temperature at ~10 K on the left side of the T_f and on the right side of T_f it shows an anomalous peak around ~70 K. From the above discussion, we can clearly say that samples C8, C9 and C10 having particle size less than 100 nm are magnetically different from the sample C11 with particle size greater than 100 nm.

5.3.3. High Temperature Structural Analysis

Fig. 5.13 demonstrates temperature dependent XRD patterns for the bulk sample (C13) of $Nd_{0.7}Ba_{0.3}Mn_{0.9}Ti_{0.1}O_3$ manganite measured at various temperatures from 300 K to 1300 K at an interval of 100 K. **Figs. 5.13**(b-d) display selected Bragg's peaks for (101), (121) and (220) reflections, respectively, which are seen to be shifted towards lower angle side with increasing measurement temperature. There is no change in the nature of the XRD peak are appearance of any new reflection on changing measurement temperature. These observations clearly indicate that all the temperature dependent XRD patterns can be indexed by using single phase orthorhombic structure with *Imma* space group similar to that at room temperature. The unit cell volume increases with increasing measurement temperature due to normal thermal expansion. Thus, we do not observe any structural phase transition at higher temperatures upto 1300K.

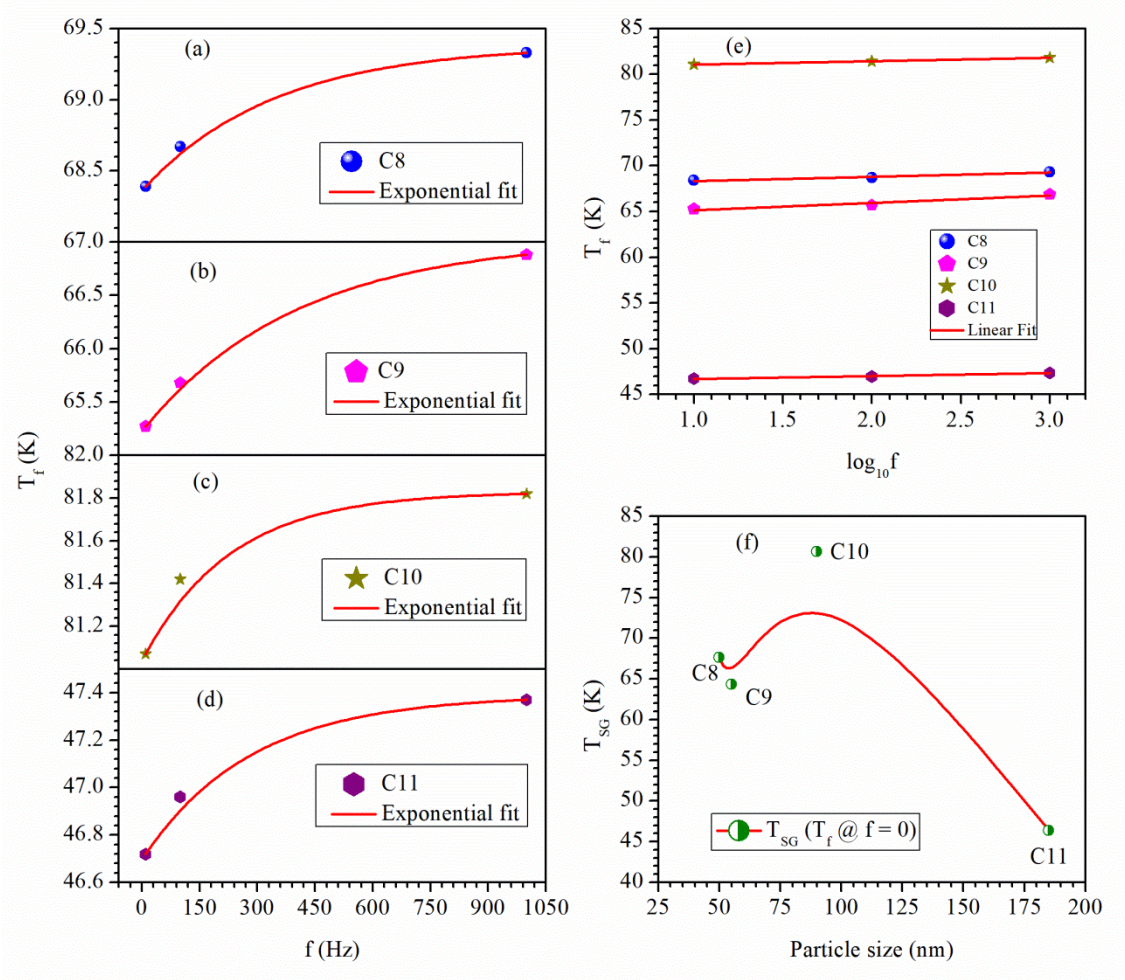

Figure 5.12: Variation in freezing temperature as a function of frequency for (a) C8, (b) C9, (c) C10 and (d) C11. (e) A plot between $\log_{10}f$ and T_f for NBMTO-10. (f) Variation in the value of T_f at zero frequency (f = 0) with respect to calcination temperature.

To find out the structural parameters from XRD patterns at different temperatures, we performed Rietveld structure refinement using orthorhombic *Imma* space group. **Figs. 5.14**(a-b) show Rietveld fits for the bulk sample (calcined at 1300°C for 6 hrs) of $Nd_{0.7}Ba_{0.3}Mn_{0.9}Ti_{0.1}O_3$ manganite for the XRD patterns recorded at 300 K and 1300 K, respectively. **Fig. 5.14**(c) shows variation in unit cell volume as a function of measurement temperature obtained from structure refinement. The unit cell volume increases continuously with measurement temperature. The lattice parameters and unit cell volume obtained from Rietveld structure refinement are listed in **Table 5.3**.

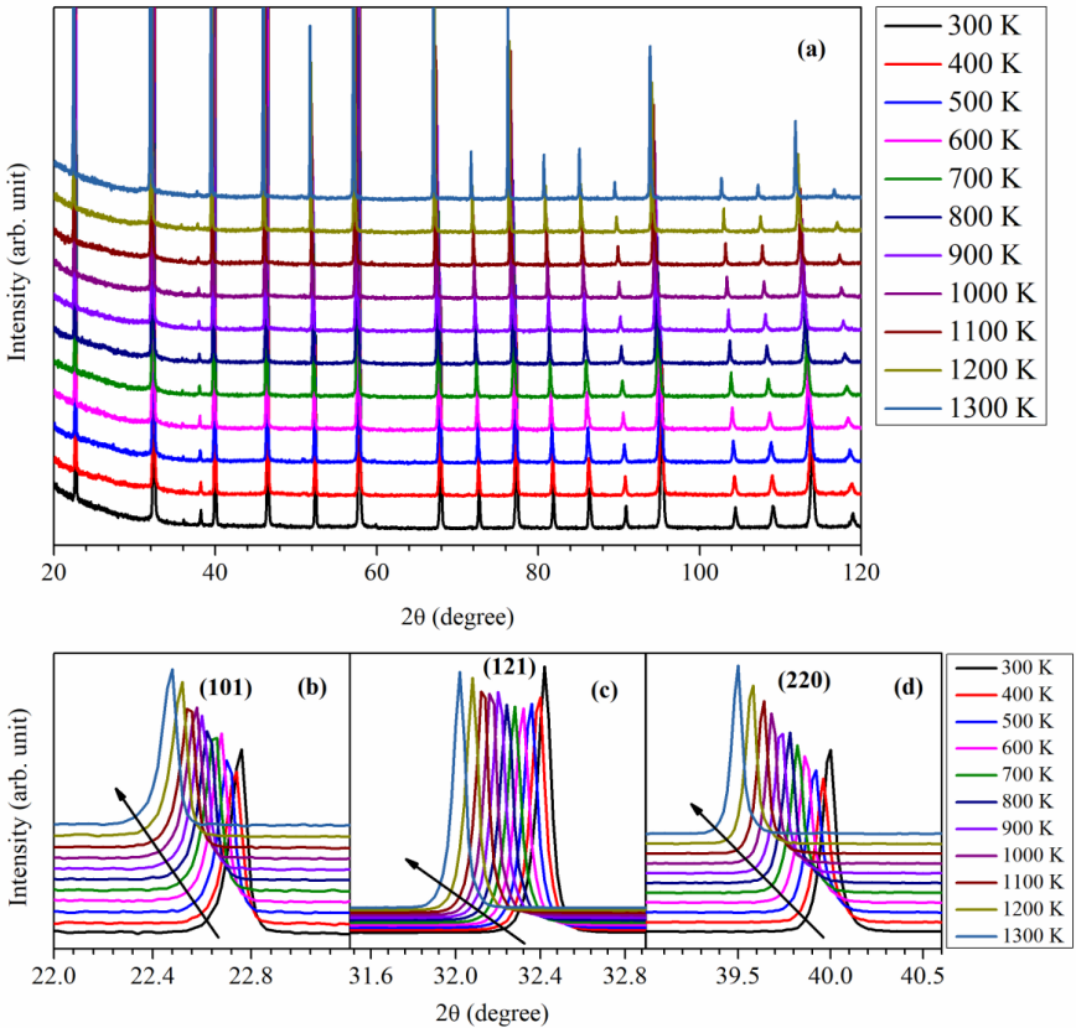

Figure 5.13: Temperature dependent XRD profiles for bulk sample of NBMTO-10 manganite measured at various temperatures. Selected Bragg's peaks for (c) (101), (d) (121), and (220) reflections corresponding to orthorhombic cell.

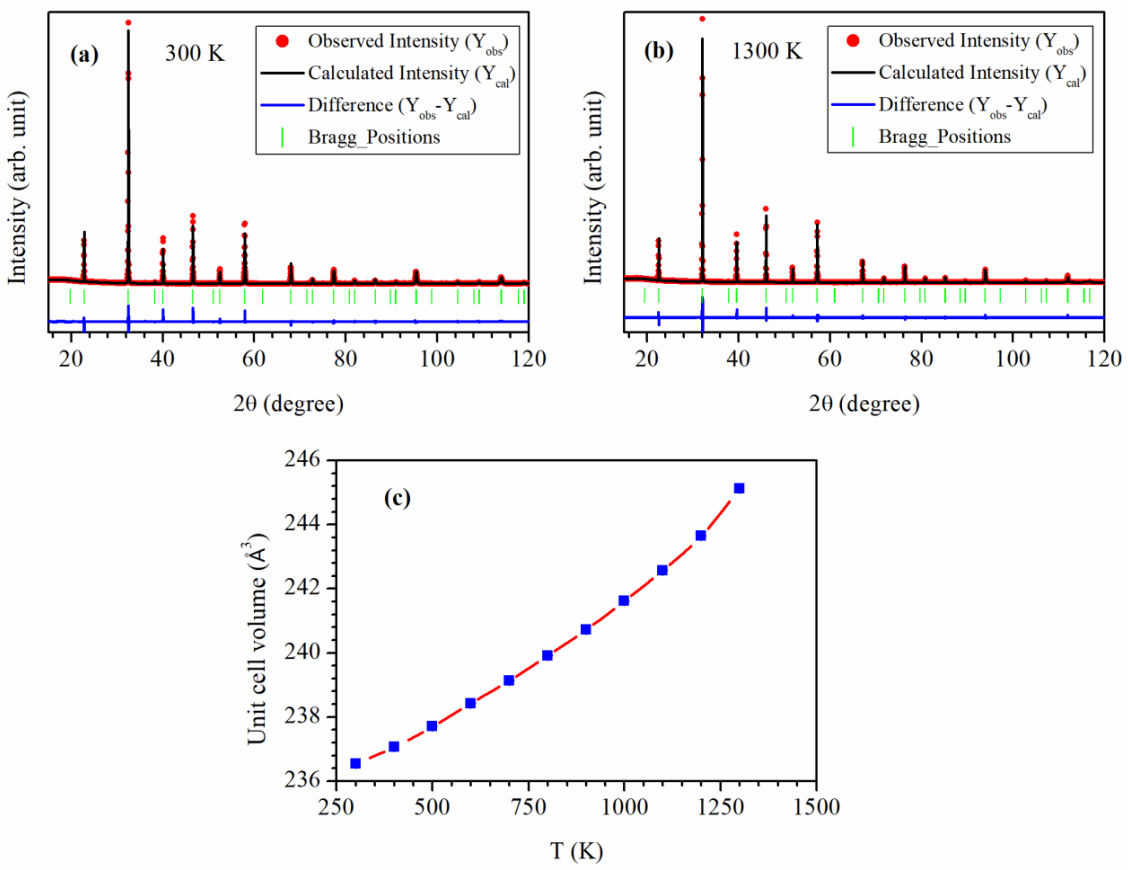

Figure 5.14: Rietveld fits for the XRD patterns of $Nd_{0.7}Ba_{0.3}Mn_{0.9}Ti_{0.1}O_3$ manganite measured at (a) 300 K and (b) 1300 K. (c) Variation in unit cell volume as a function of temperature.

Table 5.3: Lattice parameters and unit cell volume for bulk sample (C13) of $Nd_{0.7}Ba_{0.3}Mn_{0.9}Ti_{0.1}O_3$ manganite at various temperatures.

Temperature (K)	Lattice Constant (Å)			Unit Cell Volume V(Å^3)
	a	b	c	
300	5.5078(1)	7.7934(1)	5.5104(1)	236.532(6)
400	5.5122(1)	7.7989(1)	5.5145(1)	237.066(8)
500	5.5168(1)	7.8056(1)	5.5200(1)	237.705(6)
600	5.5226(1)	7.8140(1)	5.5250(1)	238.425(6)
700	5.5274(1)	7.8220(1)	5.5310(1)	239.135(6)
800	5.5329(1)	7.8307(1)	5.5372(1)	239.911(6)
900	5.5398(1)	7.8391(1)	5.5433(1)	240.729(7)
1000	5.5462(1)	7.8489(1)	5.5502(1)	241.612(7)
1100	5.5538(1)	7.8592(1)	5.5573(1)	242.570(6)
1200	5.5620(1)	7.8704(1)	5.5658(1)	243.647(6)
1300	5.5768(1)	7.8843(1)	5.5752(1)	245.132(7)

5.4. Conclusions

Pure perovskite phase nanocrystalline samples of 10 mol% Ti-doped $Nd_{0.7}Ba_{0.3}MnO_3$ manganites have been successfully prepared by the auto-combustion method. The Rietveld structure refinement of the XRD data confirms that the synthesized samples with different crystallite sizes have orthorhombic crystal structure with *Imma* space group. The values of crystallite size and particle size increase with increasing calcination temperature. However, the value of lattice strain decreases with rising calcination temperature. The unit cell volume of the samples expanded with increasing calcination temperature and enhancement in particle size. All the nanocrystalline samples of $Nd_{0.7}Ba_{0.3}Mn_{0.9}Ti_{0.1}O_3$ perovskite exhibit PM to FM phase transition at characteristic Curie temperature T_C, which shows a maximum value of 106 K for the sample C10. All the samples exhibit greater experimental effective paramagnetic moment than the theoretical value, which may be due to the existence of short-range FM ordering within the PM state. Each sample contains FM and AFM components in the low-temperature region (10 K) in which the sample C10 has a maximum percentage of FM and minimum percentage of AFM components. Shift in the field cooled magnetic hysteresis loops reveals the exchange bias effect however this effect is very small. The study of frequency dependence of magnetic ac susceptibility reveals that all the samples are exhibiting metallic spin-glass. The Rietveld structure refinement of the XRD patterns at high temperatures of bulk sample reveals no structural phase transition.